Journal of Materials Chemistry A

ROYAL SOCIETY OF CHEMISTRY

PAPER

View Article Online
View Journal | View Issue

Cite this: *J. Mater. Chem. A*, 2024, **12**, 20097

Breaking hydrogen-bonds in aqueous electrolytes towards highly reversible zinc-ion batteries†

Yilong Zhu, Qianru Chen, Junnan Hao * and Yan Jiao *

Aqueous zinc-ion batteries (AZIBs) have attracted significant attention for their potential in large-scale energy storage. However, their practical application is limited by the poor zinc reversibility because of structural deterioration and side reactions induced by water molecules. Herein, we identified pentaerythritol (PTT) as an electrolyte additive to break the H-bond network of water in the conventional aqueous $ZnSO_4$ electrolyte, after considering the cost, toxicity, conductivity, high H-bond donor number, and structure features among several options. The unique symmetry structure of PTT with four hydroxyl groups (–OH) significantly enhances its interaction with water molecules and changes the proportion of different hydrogen-bond (H-bond) types between water molecules. The introduction of PTT therefore could break the water H-bond network and change the Zn^{2+} solvation structure, as evidenced by both experimental findings and theoretical simulations. Consequently, water-induced side reactions and dendrite growth during cycling are significantly suppressed, leading to improved Zn reversibility and overall battery performance. Notable outcomes include the average coulombic efficiency reaching 99.7% and long-term stability exceeding 1000 h. This research contributes to the development of a cost-effective and efficient electrolyte strategy aimed at addressing water-induced issues in AZIBs.

Received 5th April 2024
Accepted 27th June 2024

DOI: 10.1039/d4ta02316a

rsc.li/materials-a

Introduction

The escalating demand for renewable energy sources has boosted a burgeoning market for high-performance energy storage devices in recent years.[1–3] Within this context, aqueous electrolyte-based batteries have gained significant attention due to their low flame risk and high ionic conductivity compared to those with non-aqueous electrolytes.[4,5] Particularly, aqueous Zn-ion batteries (AZIBs) have emerged as a promising alternative to traditional Li-ion batteries for large scale energy storage. The metallic Zn can be directly used as the anode because of its unique features such as a high theoretical anode capacity of 820 mA h g^{-1}, a favourable redox potential (−0.76 V *vs.* standard hydrogen electrode) and relatively low cost (AU $4.88 per kg).[6–10] In addition to the advantages offered by using zinc as the anode, the performance can be further improved by optimizing the cathode material; for example, AZIBs using vanadium-oxide-based cathodes have achieved a lifespan of 20 000 charge–discharge cycles while maintaining 91.4% of their original capacity, even at a high current density of 40.0 A g^{-1}.[11]

Despite their great potential for energy storage, one of the challenges that AZIBs face is related to the low coulombic efficiency (CE) of Zn anodes led by water-induced irreversible side reactions, including hydrogen evolution reaction (HER), corrosion reaction, by-product accumulation and Zn dendrite growth during charge and discharge cycles.[12–17] The concurrent generation of hydrogen is unavoidable in aqueous batteries given the competing HER against the Zn electrochemical deposition.[18–20] The HER also leads to an increased concentration of hydroxide ions (OH^-) near the Zn electrode surface, corroding the Zn electrode. In addition, the OH^- accumulation triggers the formation of an inactive $Zn_4SO_4(OH)_6 \cdot xH_2O$ barrier, which hinders ion/electron diffusion at the Zn/electrolyte interphase, thereby reducing the reversibility of Zn anodes.[21–25]

Various strategies have been proposed to address the challenges related to AZIBs, which include the modification of

School of Chemical Engineering, The University of Adelaide, Adelaide, 5005, Australia. E-mail: yan.jiao@adelaide.edu.au; junnan.hao@adelaide.edu.au

† Electronic supplementary information (ESI) available. See DOI: https://doi.org/10.1039/d4ta02316a

Junnan Hao

Junnan Hao received his PhD degree in 2020 from the University of Wollongong, Australia. Now he works as an ARC DECRA fellow at the University of Adelaide, Australia. His research interests are focused on energy storage and conversion, including aqueous Zn-ion batteries, high-voltage Li-ion batteries, and flexible energy storage devices.

electrolytes by adding high-concentration salts and organic additives.[26–31] For instance, a highly concentrated electrolyte (HCE) of 1 M zinc di[bis(trifluoromethylsulfonyl)imide] ($Zn(TFSI)_2$) + 20 M lithium bis(trifluoromethane)sulfonimide (LiTFSI) has been demonstrated to reduce the H_2O number in the Zn^{2+} solvation structure and suppress the side reactions.[27] However, the high viscosity of HCE leads to sluggish Zn^{2+} diffusion and poor rate capability.[32] Alternatively, a wide range of organic additives have been reported, such as methanol, dimethyl sulfoxide (DMSO), ethylene glycol (EG) and triethyl phosphate (TEP).[33–35] As a representative, methanol has been widely studied in aqueous $ZnSO_4$ electrolytes as an anti-solvent. However, since a single methanol molecule possesses only one H-bond donor, a large volume ratio (55%) is required to destroy the water H-bond network in the electrolyte. This high volume addition not only increases the cost and reduces the ionic conductivity, but also increases the risk of flammability and weakens the advantages of aqueous batteries.[36] Therefore, it is crucial to identify cost-effective additives capable of forming strong H-bonds with water molecules at low concentrations. In addition, previous research has not thoroughly explored the screening process and mechanisms at the molecular level, highlighting the importance of further investigation.

Herein, we first selected pentaerythritol (PTT) as a promising additive candidate due to its cost-effectiveness, low toxicity, high conductivity, high H-bond donor number, and unique structure features. Density functional theory (DFT) calculations were performed to demonstrate the interaction forces between additive molecules and water, with comparison to several previously reported organic alcohol additives. Results indicated that PTT with unique four symmetry hydroxyl groups (–OH) showed greater interaction with water. To investigate the dynamic impact of PTT on water molecules in the electrolyte, theoretical simulations including both classical molecular dynamics (MD) and *ab initio* molecular dynamics (AIMD) were further performed. Results demonstrated that PTT could change the coordination chemistry of Zn^{2+} by entering its solvation structure. Additionally, PTT could also break the H-bond network of water molecules and the proportion of different H-bond types between water molecules. The influence of PTT on water activity was also confirmed by experiments. The results from *in situ* gas chromatography (GC) and *ex situ* wide angle X-ray scattering (WAXS) confirmed that the water-induced side reactions and dendrite growth during cycling are significantly suppressed after adding PTT in the electrolyte. Moreover, symmetric cells assembled using the PTT-containing electrolyte exhibited stable long-term cycling over 1000 h at a current density of 1 mA cm^{-2} with a capacity of 0.5 mA h cm^{-2}. Moreover, they also exhibited a high average Zn plating/stripping CE of 99.7%. This work contributed to a cost-effective and efficient electrolyte strategy designed to tackle water-induced challenges in AZIBs.

Results and discussion

To screen a feasible additive candidate, several commonly used organic electrolyte additives were compared, such as methanol, DMSO, 1,3-dimethyl-2-imidazolidinone (DMI), EG, 1,4-dioxane (DIOXANE), *N*,*N*-dimethylformamide (DMF), and PPT. For comparison, six key parameters were selected: cost, conductivity, safety, dielectric constant, H-bond acceptor number, and H-bond donor number. To facilitate clear comparison, each parameter was normalized, as illustrated from the radar map in Fig. 1. Based on this, PTT was chosen after a thorough comparison with previously mentioned electrolyte additives. The two-dimensional structure of PTT highlights the four symmetrical hydroxyl groups, which facilitate interactions with water molecules (Fig. S1a†). Similar to the 2D diagram, the hydroxyl groups from a three-dimensional perspective are oriented in different directions, enabling PTT to interact with water from a wide range of angles (Fig. S1b†). Both figures illustrate the molecule's symmetry and the distribution of hydroxyl groups (–OH). Importantly, the unique structure of PTT (Table S1†) exhibits a highest H-bond donor number and acceptors in a single molecule among these additives, which is known to significantly impact the H-bond network of water molecules. Moreover, conductivity is a performance indicator for batteries as analysed by previous studies.[37–46] The $ZnSO_4$ electrolyte has been proven to have high biological safety and is one of the ideal zinc salts for biocompatible ZIBs.[47] The conductivity of a 2 M $ZnSO_4$ solution with 0.05 M PTT was found to be higher than that of other organic additives in the $ZnSO_4$ electrolyte (excluding the 20% DMSO volume ratio in 2 M $ZnSO_4$). In addition, considering the dielectric coefficient as an inherent physical property influencing the H-bonds in water, PTT features a high dielectric constant of 42.9, higher than those of most of the additives.

Safety assessment is based on the classification standards of the Globally Harmonized System of Classification and Labelling of Chemicals (GHS Rev.10, 2023) by the United Nations, with the acute poisoning (skin) indicator of five hazard categories used for classifying organic substances. The safety ranking reveals that PTT has a relatively less toxic category among organic additives. Moreover, cost comparison is based on quotations from the Fisher Scientific official website of Thermo Fisher Chem™ Company (AU$ per 500 ml or 500 g), revealing

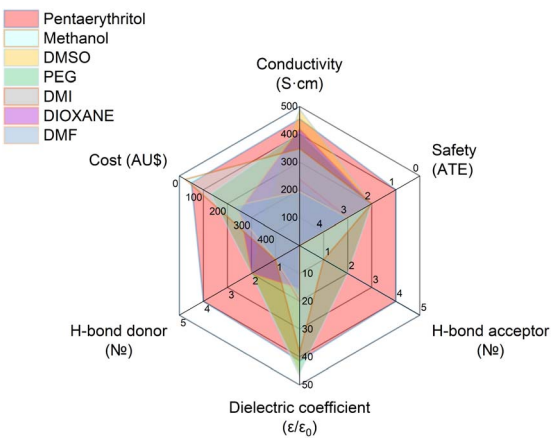

Fig. 1 Radar map screening seven different electrolyte additives for aqueous ZIBs by considering cost, conductivity, safety H-bond donor/acceptor number and dielectric coefficient.

that PTT has a relatively low cost compared to other organic additives. In summary, a comprehensive evaluation of the six parameters suggests that PTT possesses overall advantages, making it a promising choice for the electrolyte additive in ZIBs.

DFT calculations were performed to verify the interaction between additives and water molecules at a microscopic level. The interaction forces were visualized by using the independent gradient model based on the Hirshfeld partition (IGMH) method.[48] IGMH analysis in Fig. 2a–c shows regions of different interaction strengths, displayed through isosurfaces corresponding to different δ_g values (which indicates variations in electron density gradients at points of interest). Additionally, the function $\mathrm{sign}(\lambda_2)\rho$ serves as a mapping tool to distinguish interaction types. Here, r represents the genuine electron density within the current system, and a higher value signifies a stronger interaction. Moreover, l_2 is the second largest eigenvalue of the electron density Hessian matrix, with sign() retrieving the sign of a value. Therefore, positive $\mathrm{sign}(\lambda_2)$ represents repulsion while negative $\mathrm{sign}(\lambda_2)$ represents attraction. Overall, the $\mathrm{sign}(\lambda_2)\rho$ value could be used to distinguish the interaction type and intensity.

Since the height of the δ_g peak in the interaction region is positively correlated with the interaction strength, H-bonds represent the main interactions between two water molecules with an intensity of 0.05 a.u. (Fig. 2a). Similarly, the PTT molecule can also form H-bonds with a single water molecule with an intensity of 0.06 a.u., indicating higher interaction strength compared to those in pure water (Fig. 2b). Due to the high H-bond donor number of PTT (Fig. 2c), a single PTT molecule could form four stable H-bonds with water molecules, which shows that PTT molecules have strong bonding ability to attract water molecules in the electrolyte.

To evaluate the ability to bond with water, PTT and several previously reported additives were evaluated through DFT simulations, comparing their average binding energy and the average H-bond length. Here, methanol, ethanol, polypropylene (PP), glycerol, EG, and propylene glycol (PG) were selected because all of them share similar oxygen-containing groups and belong to organic alcohols (Fig. 2d). The H-bonds formed by many reported alcohol additives and water do have stronger binding energy and shorter bond length than those formed in the pure water molecules, indicating that they are able to reduce the water activity in the electrolytes (Fig. S2 and S3†). In comparison, the H-bond formed between PTT and water shows the shortest bond length and the strongest binding energy, which indicates that PTT is more promising as a potential additive candidate to reduce water activity.

Experiments were carried out to verify PTT's effectiveness for AZIBs. First, to explore the appropriate ratio of PTT, different concentrations of PTT additives (0.01–0.2 M) in 2 M $ZnSO_4$ electrolyte were prepared. After a week of standing, it was found that when the concentration of PTT added was greater than 0.05 M, solutions become turbid with precipitation, indicating improper concentration (Fig. S4†). Therefore, the concentration of 0.05 M PTT was chosen for the following MD simulation and battery performance testing. To verify the effect of PTT addition on the Zn metal anode, the polished Zn foil was soaked into the $ZnSO_4$ electrolytes containing different concentrations of PTT (Fig. 3a). After soaking for 7 days, the Zn foil was taken out and analyzed by the X-Ray diffraction (XRD) technique. As shown in Fig. 3b, the Zn foil in the pure $ZnSO_4$ electrolyte showed a significant peak at approximately 9.8°, which is indexed to the (002) plane of the $Zn_4SO_4(OH)_6\cdot xH_2O$ by-product. In contrast, the peak intensity of this corrosion by-product in the $ZnSO_4$ electrolyte with 0.05 M PTT was significantly reduced. This finding proved that the PTT additive could improve the anti-corrosion ability of Zn electrodes by reducing the activity of the electrolyte. In addition, the conductivity test showed that with the same concentration of additives, the conductivity of the $ZnSO_4$ electrolyte with methanol addition dropped by 35.2%,

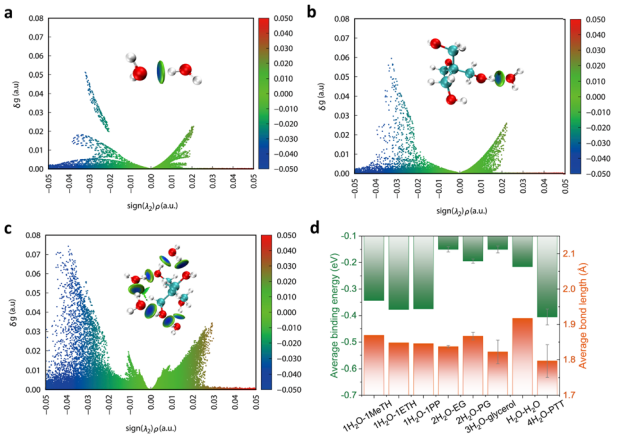

Fig. 2 Visual analysis of intermolecular interactions, (a) $1H_2O-1H_2O$, (b) $1PTT-1H_2O$, and (c) $1PTT-4H_2O$. Color code: red, O; white, H; cyan, C. (d) Average binding energy and average H-bond length between water molecules and alcohol-based additives from theoretical calculation, including methanol (MeTH), ethanol (ETH), PP, glycerol, EG, PG, and PTT.

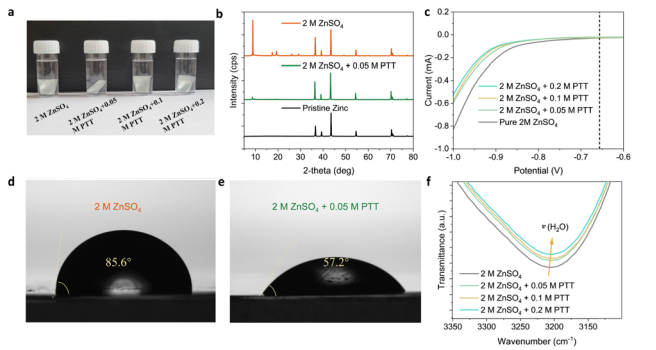

Fig. 3 Fundamental experiments on different electrolytes. (a) Snapshot of Zn foils soaking in 2 M $ZnSO_4$ electrolyte with different PTT concentrations after 7 days. (b) XRD results of the pristine Zn foil and Zn foils soaked in the pure $ZnSO_4$ electrolyte and $ZnSO_4$ with 0.5 M PTT addition. The performance of pristine Zn foil is included for comparison purposes. (c) LSV curves of the pure $ZnSO_4$ electrolyte and $ZnSO_4$ with different PTT concentrations. Snapshots of contacting angles of the pure $ZnSO_4$ electrolyte (d) and $ZnSO_4$ with 0.05 M PTT(e). (f) FTIR spectra of the pure $ZnSO_4$ electrolyte and $ZnSO_4$ with different PTT concentrations.

while the conductivity of the $ZnSO_4$ electrolyte with pentaerythritol only dropped by 4.1%, indicating that adding PTT to the $ZnSO_4$ solution has little effect on the conductivity (Fig. S5†).

To evaluate the effect of PTT on the water activity, linear sweep voltammetry (LSV) curves were measured. As shown in Fig. 3c, at the same cut-off voltage, the 0.05 M PTT-added $ZnSO_4$ electrolyte exhibited a lower current than the original $ZnSO_4$ electrolyte. This phenomenon indicates that the addition of PTT can inhibit the HER to retard the water decomposition. Additionally, the sessile drop contact angle technique was used to study the wettability of the Zn electrode in various electrolytes (using pure Zn foil as the electrode), because this feature affects the energy barrier for Zn nucleation formation and evolution. Due to its hydrophobicity, the Zn metal exhibits a high contact angle of 85.6° in the pure $ZnSO_4$ electrolyte (Fig. 3d). However, with the addition of PTT, the contact angle was significantly decreased to 57.2° (Fig. 3e). These findings emphasized the high wettability of Zn metal in the additive electrolyte because PTT has a higher adsorption than water molecules on the Zn metal surface in the additive electrolyte, thus affecting the water-induced HER and Zn nucleation formation during Zn deposition.[49] Additionally, Fourier transform infrared (FTIR) spectra of the chemical environment of H_2O in different electrolytes were collected to reveal the impact of PTT addition on H-bonds, as shown in Fig. 3f. The peak located at 3205 cm^{-1} corresponds to the strong H-bonds in H_2O.[50,51] It is worth noting that with the addition of PTT, the presence of the strong H-bonds between water molecules in the electrolyte decreased, which indicates that the addition of PTT can disturb the binding ability between water molecules.

In addition, Raman spectroscopy was utilized to investigate the changes in the H-bond network of water molecules and the solvation structure of Zn^{2+} (Fig. S6†). In the 2 M ZnSO4 with 0.05 M PTT electrolyte, the vibration peak of $[Zn^{2+}\cdot OH_2]$ shifted from 390 cm^{-1} to 382 cm^{-1} compared to the peak in the 2 M $ZnSO_4$ electrolyte, indicating that the typical solvation structure of the $[Zn(H_2O)_6]^{2+}$ complex was suppressed (Fig. S6a†). This implies that PTT addition influences Zn^{2+} solvation, lowering the energy barrier for Zn^{2+} detachment. Moreover, the intensity peak of $[HOH\cdot OH_2]$ between 3264–3304 cm^{-1} in the 2 M $ZnSO_4$ with 0.05 M PTT electrolyte was also lower than in the 2 M $ZnSO_4$ electrolyte (Fig. S6b†), indicating weaker H-bond strength between water molecules. This suggests that PTT disrupts water H-bonds, facilitating Zn^{2+} transport in the battery. Similarly, the reduced intensity of the $[HOH\cdot OSO_3{}^{2-}]$ vibration between 3387–3416 cm^{-1} indicates decreased H-bond strength between water and $SO_4{}^{2-}$, reflecting stronger PTT–water interaction. These results above demonstrate the PTT effects on the hydrogen bonding network of water molecules and the solvation structure of Zn^{2+}.

To further explore the impact of PTT on the $ZnSO_4$ electrolyte at the atomic level, theoretical calculations were carried out to simulate the pure $ZnSO_4$ electrolyte environment and $ZnSO_4$ electrolyte with PTT addition (Table S2†). As shown in Fig. 4a and S7†, after relaxation for 100 ns, each component is evenly distributed in the $ZnSO_4$ aqueous solution system. Moreover, with the presence of PTT in the electrolyte, as shown in the

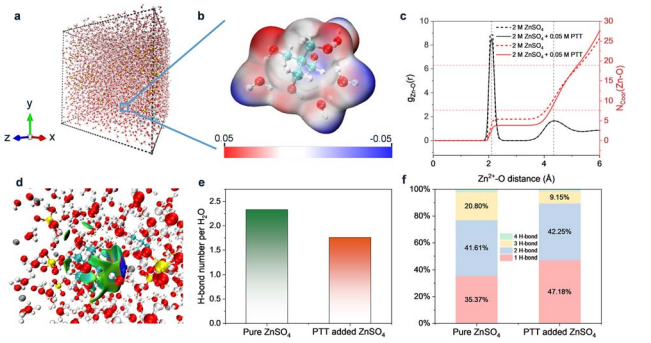

Fig. 4 Theoretical MD simulation and analyses. Snapshot of (a) the model for pure $ZnSO_4$ with 0.05 M PTT (b) the Electrostatic Potential (ESP) map of one PTT molecule with four water molecules. (c) $N_{coor.}$ and $g(r)$ of 2 M $ZnSO_4$ and 2 M $ZnSO_4$ with 0.05 M PTT between Zn^{2+} and the first solvation sheath (last 5 ns within equilibrium simulations). (d) Snapshot of the intermolecular interactions between PTT and surrounding $ZnSO_4$ molecules in the model of 2 M $ZnSO_4$ with 0.05 M PTT. (e) The average H-bonds of two electrolyte systems. (f) Proportion of each H-bond type between water molecules of two electrolyte systems. Color code: red, O; white, H; yellow, S; cyan, C; grey, Zn.

partially enlarged solvation sheath structure in Fig. 4b, PTT molecules can form H-bonds with water molecules. Moreover, the Zn^{2+} solvation structure changes after adding the additive, as confirmed by the radial distribution function (RDF, *i.e.* $g(r)$) and coordination number ($N_{coor.}$) of Zn^{2+} with the oxygen in water or the additive (Fig. 4c). Results showed that the addition of PTT decreased the water molecules' coordination number from 5.3 to 4.1 in the first solvation sheath of Zn^{2+}. This is also confirmed by the AIMD results. The root mean square deviation (RMSD) of the two systems shows that the addition of PTT could change the solution environment, which verifies that PTT contributes to the reshaping of the Zn^{2+} solvation structure as well. Additionally, the intermolecular interactions between PTT and surrounding $ZnSO_4$ molecules in the model of 2 M $ZnSO_4$ with 0.05 M PTT were investigated. As shown in Fig. 4d, the PTT molecule interacts with the Zn^{2+} and surrounding water molecules. The interaction is represented by the δ_g isosurface values (same color scale as in Fig. S8†), which indicates variations in electron density gradients at points of interest. Among them, the green isosurface represents the dispersion force, which is related to the van der Waals interaction, while the navy blue isosurface represents the prominent attractive interaction. This figure suggests that Zn^{2+} has a contribution to attracting PTT into the solvation sheath. Moreover, the PTT molecule in the system can also interact with surrounding water molecules without Zn^{2+} (Fig. S8†), which proves that PTT molecules not only can form H-bonds with water molecules, but also have a high strength attraction with Zn^{2+}, thus affecting the solvation sheath of Zn^{2+}. These findings indicate that the addition of PTT can affect the Zn^{2+} solvation equilibrium, leading to the desolvation and rapid transport of Zn^{2+} with a low energy barrier.[28,52,53]

As shown in Fig. 4e, among the two models that contain the same number of water molecules, the average number of H-

bonds per H_2O in pure $ZnSO_4$ solution is about 2.3. As for the $ZnSO_4$ solution with PTT added, the average number of H-bonds was reduced to 1.7, which was a 28% reduction compared with the pure $ZnSO_4$ solution. This confirmed that the original water–water H-bond network was disrupted, therefore indicating that the addition of PTT can effectively reduce the water molecules' activity, and thereby inhibit the HER. These simulation results were consistent with the experimental results (Fig. 3c). In addition, Fig. S9† shows the classification of H-bond numbers between water molecules; for example, the 1-H-bond means that the water molecule only contributes to one H-bond, and the 4-H-bond means that both H atoms and O atoms in the water molecules contribute to the formation of the H-bonds. In aqueous solutions, stronger H-bonds between water molecules result in a robust hydrogen bonding network that impedes the transport of Zn^{2+}.

Additionally, water molecules tend to accumulate on the surface of the negative electrode during the charging progress, leading to the HER. By analyzing the classification of different numbers of H-bonds between water molecules, the types of 1-H-bond and 2-H-bond are related to the weak H-bond, while the types of 3-H-bond and 4-H-bond are related to the strong H-bond. As shown in Fig. 4f, the types of 1-H-bond and 2-H-bond in pure $ZnSO_4$ accounted for 35.37% and 41.61%, respectively. The 3-H-bond and 4H-bond accounted for 20.8% and 2.22%, respectively. In contrast, in the $ZnSO_4$ with 0.05 M PTT, the proportion of 1-H-bond type and 2-H-bond increased to 47.18% and 42.25%, respectively. The proportion of 3-H-bond and 4-H-bond dropped to 9.15% and 1.42%, respectively. Due to the interference of PTT on the H-bond between water molecules, some of the strong H-bonds were converted into weak H-bonds.[54] Additionally, some PTT molecules will replace water molecules on the surface of the negative electrode, thereby inhibiting the occurrence of the HER. The changes proved that the addition of PTT can significantly break the H-bond network of the $ZnSO_4$ electrolyte by affecting the number and type of H-bonds of water molecules in the solution, which is beneficial in reducing the HER in the solution and improving the Zn^{2+} transmission efficiency.

Electrochemical characterization was performed to evaluate the CE of Zn stripping/plating with different electrolytes. The reversibility of Zn chemistry was studied by conducting plating/stripping measurements on Zn//Cu coin cells at 1 mA cm^{-2} and 0.5 mA h cm^{-2}. As shown in Fig. 5a, the Zn//Cu cell using the 2 M $ZnSO_4$ electrolyte achieved an average CE of 97.8% in the first 170 cycles. The CE value fluctuated in subsequent cycles due to the cell failure, which is mainly related to interfacial passivation caused by dendrite deposition, HER and $Zn_4SO_4(OH)_6\cdot xH_2O$ by-products.[55] In contrast, Zn//Cu cells with the addition of PTT showed significantly improved CE. Specifically, the Zn//Cu cell showed higher CE in the first 10 h and remained stable after 1000 h. Importantly, this Zn//Cu battery exhibited a higher average CE of approximately 99.68%, which is attributed to the reduced water molecule activity with PTT. When the current density increased to 5 mA cm^{-2}, the cell with the 2 M $ZnSO_4$ electrolyte had an average CE of 98.7%. In contrast, the $ZnSO_4$ electrolyte with 0.05 M PTT addition still exhibited high

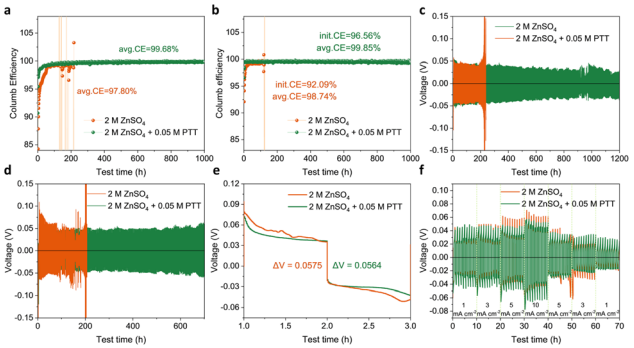

Fig. 5 Coulombic efficiency of Zn//Cu cell plating/stripping in the pure $ZnSO_4$ electrolyte and $ZnSO_4$ with 0.05 M PTT: (a) at 1 mA cm^{-2} and a capacity of 0.5 mA h cm^{-2}, (b) at 5 mA cm^{-2} and a capacity of 2.5 mA h cm^{-2}. The cycling lifespan of Zn//Zn symmetric cells in the pure $ZnSO_4$ electrolyte and designed electrolyte: (c) at 1 mA cm^{-2} and a capacity of 0.5 mA h cm^{-2}, (d) at 5 mA cm^{-2} and a capacity of 2.5 mA h cm^{-2}. (e) The first charge/discharge cycle of Zn//Zn symmetric cells. (f) Rate capability of Zn//Zn symmetric cells under different current densities from 1 mA cm^{-2} to 10 mA cm^{-2}.

Zn reversibility, with an average CE of 99.85% over 1000 h (Fig. 5b). These findings show that compared to the pure $ZnSO_4$ electrolyte, the $ZnSO_4$ electrolyte with PTT addition shows better electrochemical stability in stripping/plating.

Zn//Zn symmetric cells were assembled to test the effect of adding PTT on the cycling life and stability of Zn anode plating/stripping. At the current density of 1 mA cm^{-2}, the voltage of the cell in the pure $ZnSO_4$ electrolyte dropped significantly after about 230 h, indicating that the battery failed due to the occurrence of short circuit (Fig. 5c). Additionally, under the same conditions, the cell with the $ZnSO_4$ electrolyte containing PTT showed superior cycle stability with a lifespan of over 1000 h. At 5 mA cm^{-2}, the voltage of the cell in the pure $ZnSO_4$ electrolyte became unstable after 150 h, indicating battery failure. However, the cell with the 0.05 M PTT added $ZnSO_4$ electrolyte also had a lifespan over 700 h (Fig. 5d). Additionally, from the first charge/discharge cycle, the curves of the $ZnSO_4$ with PTT addition are smoother. However, the polarization of the cells with different electrolytes is similar under low current density. Fig. 5f shows the rate performance of symmetric cells with the pure $ZnSO_4$ electrolyte and the $ZnSO_4$ with PTT electrolyte for 1 h per cycle at current densities of 1, 3, 5, and 10 mA cm^{-2}, respectively. It can be seen that the symmetrical cell using $ZnSO_4$ with PTT has lower polarization than that using the pure $ZnSO_4$ electrolyte under high current densities, *e.g.* 5 mA cm^{-2}. These findings indicated that PTT could promote stable and efficient operation of Zn-based batteries.

To further investigate the reason why PTT can improve the Zn reversibility, Zn electrodes stripped from cells with different electrolytes were evaluated after the 100th plating cycle. XRD measurements were performed to study the deposition behavior of Zn electrodes after cycling. In the $ZnSO_4$ electrolyte, the Zn electrode showed a significant peak at approximately 9.8° (Fig. 6a), pointing to the (002) plane of the $Zn_4SO_4(OH)_6\cdot xH_2O$ by-product. This finding confirmed that significant corrosion

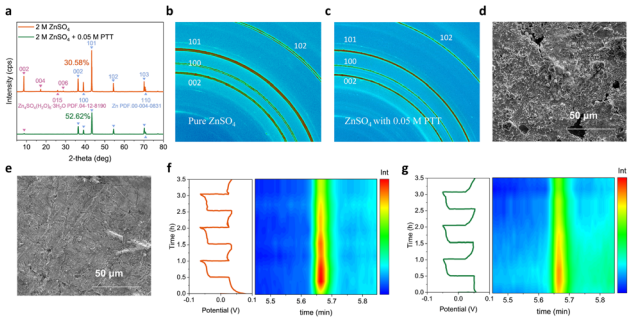

Fig. 6 Zn plating behaviour studies. (a) XRD patterns of Zn electrodes after 100th plating in the pure $ZnSO_4$ electrolyte and the $ZnSO_4$ with PTT electrolyte. WAXS of the Zn electrode in the $ZnSO_4$ electrolyte (b) and $ZnSO_4$ with PTT addition (c) after the 100th plating. SEM images of Zn electrodes in different $ZnSO_4$ electrolytes: after the 100th plating in the pure $ZnSO_4$ electrolyte (d) and in the $ZnSO_4$ electrolyte with PTT addition (e). *In situ* GC curves to dynamically evaluate the H_2 amount during the Zn plating/stripping (f) in the pure $ZnSO_4$ electrolyte and (g) in the $ZnSO_4$ electrolyte with PTT addition.

occurs during battery cycling. In contrast, a significantly reduced peak appeared at about 9.8° in the XRD pattern of the Zn electrode after cycling in the $ZnSO_4$ with 0.05 M PTT, indicating that the deposition orientation of the Zn electrode was significantly changed. These results help to improve the Zn reversibility in the electrolyte. Furthermore, for the Zn electrode in the pure $ZnSO_4$ electrolyte, the peak intensity ratio of Zn(002)/Zn(101) was 30.58%. But for the Zn electrode in the $ZnSO_4$ with 0.05 M PTT, the peak intensity ratio of Zn(002)/Zn(101) increased to 52.62%, indicating that PTT changes the preferred orientation for Zn (002) deposition. It has been widely accepted that the Zn (002) deposition helps to suppress the dendrite growth. In addition, WAXS measurements were performed to verify the deposition orientation of Zn electrodes after cycling. For the Zn electrode in the pure $ZnSO_4$ electrolyte, the (101) plane showed a significant scattering peak intensity (Fig. 6b). As a comparison, the Zn electrode in the $ZnSO_4$ electrolyte with PTT addition showed a decreased scattering peak intensity of the (101) plane while an increased peak for the (002) plane. This suggests the change of the Zn deposition direction in the $ZnSO_4$ electrolyte with PTT addition as well (Fig. 6c). In contrast, in the $ZnSO_4$ electrolyte added with PTT, the peak of the (002) plane of the Zn electrode appears significantly reduced, confirming that the deposition orientation of the Zn electrode was significantly changed, which is consistent with XRD results. In addition, the one-dimension of intensity counts showed the same results (Fig. S10†). It was observed from scanning electron microscopy (SEM) images that the surface of the stripped Zn electrode with the pure $ZnSO_4$ electrolyte was corroded after 100th cycled plating/stripping at a current density of 1 mA cm^{-2} with a capacity of 0.5 mA h cm^{-2}, with a large number of byproducts (such as $Zn_4SO_4(OH)_6 \cdot xH_2O$) and holes found on the Zn electrode surface, resulting in limited reversibility of Zn in the $ZnSO_4$ electrolyte (Fig. 6d). In comparison, the Zn electrode after cycling in the $ZnSO_4$ with PTT addition exhibited a clean and uniform surface; there are no obvious holes or by-products found (Fig. 6e).

Chronoamperometry (CA) tests were performed on an electrochemical workstation; the change of current with time at a constant potential can sensitively reflect the nucleation process and surface changes (Fig. S11†). At a constant voltage of −150 mV, measured by CA, the current density for the coin cell using the pure 2 M $ZnSO_4$ electrolyte continued to decrease over 150 s. This indicates ongoing 2D diffusion processes and rough deposition propagation. Zn^{2+} ions tend to aggregate and grow into dendrites to minimize the surface energy and exposed area. The current curve for 2 M $ZnSO_4$ with 0.05 M PTT shows an almost constant value at −30 mA cm^{-2} after a brief 2D diffusion period of 20 s, reflecting a prolonged 3D compact diffusion process after nucleation. These results suggest that PTT can be beneficial for Zn surface deposition. This result shows the inhibition of the corrosion for the Zn electrolyte when adding PTT into the $ZnSO_4$ electrolyte. It was observed from cyclic voltammetry (CV) tests that the nucleation overpotential (NOP) is the potential difference between the intersection point (A) and the point (B/B′), where Zn^{2+} ions begin to reduce on the substrate (Fig. S12†). It is considered a convenient parameter to explain the degree of polarization and shows the effect of electrode modification.[56–59] Compared with the Zn/Cu battery using the pure $ZnSO_4$ electrolyte, the Zn/Cu battery using the 2 M $ZnSO_4$ with 0.05 M PTT electrolyte improved the NOP by 10 mV (−30 mV to −40 mV). This increased overpotential provides sufficient driving force for the nucleation and growth process of finer nuclei.[60] In addition, the current density of the coin cell using 2 M $ZnSO_4$ with 0.05 M PTT is higher compared to that of the coin cell using the pure $ZnSO_4$ electrolyte, indicating that the latter has high electrochemical reactivity and higher capacity. Such observations clearly demonstrate the positive role of adding PPT in regulating the Zn deposition. The results from Energy Dispersive X-Ray Spectroscopy (EDX) analysis also confirmed that there are fewer by-products found in the stripped Zn electrode with the PTT addition (Fig. S13†). This finding also confirmed that the corrosion of the Zn electrode is significantly inhibited after the addition of PTT.

In addition, *in situ* GC analysis was conducted to dynamically assess hydrogen release during battery operation. As shown in the contour plots in Fig. 6f and g, the highest amount of H_2 produced in the pure $ZnSO_4$ aqueous electrolyte was 58.03 ppm during the repeated Zn plating/stripping process at a current density of 5 mA cm^{-2} (Fig. 6f). In the $ZnSO_4$ electrolyte with PTT addition, the intensity of hydrogen release was significantly suppressed (Fig. 6g). The one-dimensional *in situ* GC curves are shown in Fig. S14†. By comparison, the dynamic hydrogen release of the $ZnSO_4$ electrolyte with PTT addition decreased by 44.5%, indicating that the HER was significantly inhibited, which contributes to the enhancement of Zn reversibility.

Moreover, we assembled Zn–I_2 full cells with/without the additive and tested their electrochemical performance, such as charge/discharge curves and cycling performance (Fig. S15†). As shown in Fig. S15a†, for the representative charge/discharge curves, the cell containing the 2 M $ZnSO_4$ with 0.05 M PTT electrolyte demonstrates a higher CE of 92.7%, compared to

85.2% for the Zn–I_2 cell with pure 2 M $ZnSO_4$. This indicates that the addition of PTT enhances the charge/discharge reversibility of the Zn–I_2 battery. Cycling performance was assessed to demonstrate the PTT effect. While having a higher CE, the Zn–I_2 cell containing the 2 M $ZnSO_4$ with 0.05 M PTT electrolyte also achieves a higher capacity retention of 98.9% compared to 86.2% for the cell with the pure $ZnSO_4$ electrolyte after 200 cycles at 0.2 A g^{-1} (Fig. S15b†). It shows that the addition of PTT significantly inhibits the shuttling effect of polyiodide anions (I_3^-/I_5^-). These results indicate that the addition of PTT can achieve a highly reversible and shuttle-free Zn–I_2 battery and prolong the battery lifespan.

Conclusions

In summary, we screen a promising electrolyte additive for sustainable AZIBs and provide atomic-level insights into exploring its impact on electrolyte performance by combining experiments and theoretical calculations. PTT has a unique symmetrical structure with four hydroxyl groups (–OH), which significantly enhances its interaction with water molecules and changes the ratio of different H-bond types (strong H-bonds decrease and weak H-bonds increase) between water molecules. These results prove that PTT as an additive can break the H-bond network of water molecules and change the solvation structure of Zn^{2+}, thereby suppressing dendrite growth and side reactions on the Zn anode during cycling. As a result, water-induced side reactions and dendrite formation during cycling are significantly reduced, resulting in improved Zn reversibility and overall battery efficiency. Notable outcomes include the average CE reaching 99.7% and long-term stability exceeding 1000 h. This study contributes to the development of cost-effective and efficient electrolyte strategies aimed at solving the problems caused by water in AZIBs.

Methods

Experimental

Materials. Zn foil, a three-electrode cell, Cu foil, an Ag/AgCl electrode, hydrophobic polytetrafluoroethylene (PTFE), and a Pt electrode were purchased from Shenzhen Kejing Star Technology. $ZnSO_4 \cdot 7H_2O$ (≥99.0%), sodium iodide (≥99.5%), and pentaerythritol (anhydrous, 98%) were purchased from Sigma-Aldrich Chemical Co. All other reagents were of analytical grade and used directly without purification. Deionized water was used to prepare all aqueous electrolytes.

Electrolyte preparation. To prepare a series of solutions, $ZnSO_4 \cdot 7H_2O$ was dissolved directly in water. To obtain the target concentration (2 M), the appropriate amount of $ZnSO_4 \cdot 7H_2O$ was gradually and slowly added in water by sonication and intermittent strong shaking. For the PTT added $ZnSO_4$ electrolytes, the masses of PTT powder were first calculated and weighed corresponding to the target concentration (0.01–0.2 M), and then gradually dissolved in the prepared 2 M $ZnSO_4$ electrolyte respectively.

Material characterization. The crystal structure of the Zn electrode was studied by X-Ray diffraction (XRD, PANalytical X-Ray diffractometer) using Cu Kα radiation and a scan rate of 5° min^{-1}. The morphology of the Zn electrode after different cycles was observed by scanning electron microscopy (SEM, Quanta450). Contact angles between the Zn electrode and 2 M $ZnSO_4$ electrolyte were collected on a Dataphysics OCA15 apparatus with 1 μL of electrolyte for each test. FTIR spectra of different electrolytes were acquired using a PerkinElmer leading edge Fourier transform infrared (FTIR) spectrometer (PerkinElmer) in the range 4000–400 cm^{-1}. Gas chromatography (GC, Agilent 8890B) was used to collect *in situ* the gases generated during the galvanizing/stripping process. *Ex situ* WAXS were recorded using a Bruker-AXS Micro-diffractometer (D8 ADVANCE) with $CuK_{\alpha 1}$ radiation ($\lambda = 1.5405$ Å).

Electrochemical tests were carried out using CR 2032 coin-type cells with glass fiber filters serving as separators. Prior to usage, the Zn foil underwent polishing using softback sanding sponges (3M, USA) and was subsequently wiped with ethanol. Unless specified otherwise, Zn anodes were cut into disk-shaped electrodes with a 10 mm diameter for coin cell assembly. The volume of electrolyte addition was 70 μL for coin cells and 100 μL for the full cells. The volume was meticulously measured using a calibrated pipette to maintain high accuracy and repeatability across all experimental runs. Charge–discharge tests for coin cells were conducted using the LAND battery test system (CT2001A). For intermittent charge/discharge tests, Zn//Zn cells were sequentially charged/discharged at a current density of 1 mA cm^{-2}, reaching a total capacity of 0.5 mA h cm^{-2}. Zn//Cu asymmetric cells were subjected to charge–discharge cycles at 1 mA cm^{-2}, with a capacity of 0.5 mA h cm^{-2} and an upper cut-off voltage of 0.8 V. These cycles were employed to assess the CE of different electrolytes.

LSV curves of $ZnSO_4$ were collected using a three-electrode system, in which the glycerol electrode was used as the reference electrode, and stainless steel was used as the working electrode and counter electrode. The test was performed on an electrochemical working station CHI 760E within a voltage range from 0 V to −1.6 V with a scan rate of 1 mV s^{-1}. Chronoamperometry was performed on Zn//Zn symmetric batteries on a CHI760E with a constant step potential of −150 mV. Raman spectra were collected with Labram HR Evolution (Horiba Scientific) using a 532 nm laser.

DFT and energy calculations. DFT was used to study the interaction energies between water and pentaerythritol (H_2O–H_2O, H_2O–PTT and $4H_2O$–PTT. All structures were optimized by DFT based on the B3LYP-D3(BJ) mixed functional and 6−311+G* basis sets, using the Gaussian G09RevD.01 program.[61] Single-point energy calculations were performed for each optimized structure by using 6−311+G** basis sets.[62] The electrostatic potential (ESP) was measured using Multiwfn (v. 3.8) and rendered by VMD (v. 1.9.3),[63,64] which also served as a visualization tool, along with gnuplot (v. 5.2).[65] IGMH analysis was carried out using Gaussian and Multiwfn 3.8.[63] Since the effect of interactions (such as H-bonds) did not involve chemical bond formation and breaking reactions, the inter-molecular interaction energy was needed in terms of this work. Normally, the interaction energy ($E_{interaction}$) describes the energy change between two molecules. Considering that the basis set

overlapped in the solvated structural system, this part of the contribution was removed for precise results by Basis Set Superposition Error (BSSE) compensation.[66] Here, the counterpoise method (for BSSE correction) was used when performing the DFT calculation to correct the interaction energy. After DFT calculation, the interaction energy could be obtained from the equation: $E_{\text{interaction}} = E_{\text{total}} - E_{H_2O} - E_{\text{single molecule}} + E_{\text{BSSE}}$. Total represents the stable molecular group after structural optimization, including H_2O and single molecules, and the additive molecule represents one H_2O, MeTH (methanol), ETH (ethanol), PP (polypropylene), EG (ethylene glycol), PG (propylene glycol), glycerol and PTT molecule, respectively.

MD simulation. The classical MD simulations were performed on both pure $ZnSO_4$ electrolyte and the 0.05 M PTT added 2 M $ZnSO_4$ electrolyte. Simulations were carried out using the NAMD package to investigate the solvation structure of electrolytes.[67] The solution model contained different numbers of $ZnSO_4$, water molecules and additives (as shown in Table S2†). Table S3† shows the periodic boundary size of different system cells after a 100 ps minimization and a 10 ns constant temperature and pressure (NPT) simulation at 300 K and 1 atm.

The forced field parameters for PTT, Zn^{2+} and SO_4^{2-} were obtained from CHARMM36 force fields.[68] The TIP3P water model was employed for H_2O.[69] The time step was set to be 2 fs. The cutoff radius for vdW was 12 Å and the electrostatic interactions were 10 Å. The standard periodic boundary condition was used in all simulations. After minimization of the initial structure for 50 000 steps (100 ps), each system was heated from 100 K to 300 K by performing Langevin dynamics temperature control for 0.8 ns (400 000 steps). The systems were further relaxed for another 9.2 ns under NPT by the Nosé–Hoover Langevin piston pressure control method[70] at 1.01325 bar. After relaxation, each system was simulated for 100 ns under the canonical ensemble (NVT) for data collection and statistical analysis.[71]

AIMD simulations were performed with the CP2K computational suite (v. 2023.1),[72] employing the DFT representation of the electronic structure, which is integrated within the Quickstep module of CP2K.[73] The Perfect Bayesian Equilibrium (PBE) exchange–correlation functional[74] was used.[75] The molecularly optimized short-ranged double-zeta (DZVP-MOLOPT-SR-GTH) basis set for atomic orbitals was utilized,[76] coupling with the auxiliary plane wave expansion of the electron density up to a 400 Ry cutoff. Core electrons were depicted using norm-conserving GTH pseudopotentials tailored for the PBE functional.[77] Additionally, smoothing of the electron density and its derivative on the spatial integration grid was implemented (*via* keywords XC_SMOOTH_RHO NN50 and XC_DERIV NN50_SMOOTH in CP2K), as previous findings indicated a notable enhancement in the stability of local energetics for liquid water.[78] Dispersion effects were accounted for using a two-body DFT-D3 empirical dispersion correction, with zero damping terms and a cutoff set to 10 Å.[79]

The 2 M $ZnSO_4$ electrolyte system contained 200 water molecules, 20 Zn^{2+} ions and 20 SO_4^{2-} anions. And the system of 2 M $ZnSO_4$ with 0.05 M PTT contained 200 water molecules, 20 Zn^{2+}, 20 SO_4^{2-} and 1 PTT molecules. Each system was first equilibrated for 0.5 ps in an AIMD simulation in the NPT ensemble at $T = 298.15$ K, and the simulation time step was set to be 1 fs. After this equilibration period, the NVT ensemble was continued for 10 ps, with data collection every 1 fs. All MD analyses were performed using the VMD software package (v. 1.9.3).[64]

Data availability

The data supporting this article have been included as part of the ESI.†

Conflicts of interest

The authors declare no conflict of interest.

Acknowledgements

We acknowledge financial support by the Australian Research Council (FT190100636 and DE230100471). MD computations within this research were undertaken with the assistance of resources and services from the Phoenix High Performance Computing (HPC), which is supported by The University of Adelaide. DFT computations were undertaken with the assistance of resources and services from the National Computational Infrastructure (NCI), which was supported by the Australian Government. We would like to thank Yanzhang Zhao for his contribution to developing the code for H-bond analysis from AIMD results.

Notes and references

1 M.-C. Lin, M. Gong, B. Lu, Y. Wu, D.-Y. Wang, M. Guan, M. Angell, C. Chen, J. Yang and B.-J. Hwang, *Nature*, 2015, **520**, 324–328.
2 H. Pan, Y. Shao, P. Yan, Y. Cheng, K. S. Han, Z. Nie, C. Wang, J. Yang, X. Li and P. Bhattacharya, *Nat. Energy*, 2016, **1**, 1–7.
3 Y. Liu, A. Gao, J. Hao, X. Li, J. Ling, F. Yi, Q. Li and D. Shu, *Chem. Eng. J.*, 2023, **452**, 139605.
4 C. Zhong, B. Liu, J. Ding, X. Liu, Y. Zhong, Y. Li, C. Sun, X. Han, Y. Deng and N. Zhao, *Nat. Energy*, 2020, **5**, 440–449.
5 L. Kang, J. Zheng, K. Yue, H. Yuan, J. Luo, Y. Wang, Y. Liu, J. Nai and X. Tao, *Small*, 2023, **19**, 2304094.
6 J. Zheng, Q. Zhao, T. Tang, J. Yin, C. D. Quilty, G. D. Renderos, X. Liu, Y. Deng, L. Wang and D. C. Bock, *Science*, 2019, **366**, 645–648.
7 X. Zeng, J. Mao, J. Hao, J. Liu, S. Liu, Z. Wang, Y. Wang, S. Zhang, T. Zheng and J. Liu, *Adv. Mater.*, 2021, **33**, 2007416.
8 C. Li, S. Jin, L. A. Archer and L. F. Nazar, *Joule*, 2022, **6**, 1733–1738.
9 R. Zhao, H. Wang, H. Du, Y. Yang, Z. Gao, L. Qie and Y. Huang, *Nat. Commun.*, 2022, **13**, 3252.
10 C. Yang, J. Xia, C. Cui, T. P. Pollard, J. Vatamanu, A. Faraone, J. A. Dura, M. Tyagi, A. Kattan and E. Thimsen, *Nat. Sustain.*, 2023, **6**, 325–335.

11 S. Deng, Z. Yuan, Z. Tie, C. Wang, L. Song and Z. Niu, *Angew. Chem., Int. Ed.*, 2020, **59**, 22002–22006.
12 J. Fu, D. U. Lee, F. M. Hassan, L. Yang, Z. Bai, M. G. Park and Z. Chen, *Adv. Mater.*, 2015, **27**, 5617–5622.
13 M. Xu, D. Ivey, Z. Xie and W. Qu, *J. Power Sources*, 2015, **283**, 358–371.
14 Z. Liu, T. Cui, G. Pulletikurthi, A. Lahiri, T. Carstens, M. Olschewski and F. Endres, *Angew. Chem., Int. Ed.*, 2016, **55**, 2889–2893.
15 X. Zeng, J. Hao, Z. Wang, J. Mao and Z. Guo, *Energy Storage Mater.*, 2019, **20**, 410–437.
16 Z. Li and A. W. Robertson, *Battery Energy*, 2023, **2**, 20220029.
17 J. Chen, Z. Yan, K. Li, A. Hu, B. Yang, T. Li, M. He, Y. Li, Z. Wei Seh and J. Long, *Battery Energy*, 2024, **3**, 20230063.
18 Q. Yang, G. Liang, Y. Guo, Z. Liu, B. Yan, D. Wang, Z. Huang, X. Li, J. Fan and C. Zhi, *Adv. Mater.*, 2019, **31**, 1903778.
19 L. Ma, M. A. Schroeder, O. Borodin, T. P. Pollard, M. S. Ding, C. Wang and K. Xu, *Nat. Energy*, 2020, **5**, 743–749.
20 Q. Zhang, J. Luan, Y. Tang, X. Ji and H. Wang, *Angew. Chem., Int. Ed.*, 2020, **59**, 13180–13191.
21 J. Hao, X. Li, X. Zeng, D. Li, J. Mao and Z. Guo, *Energy Environ. Sci.*, 2020, **13**, 3917–3949.
22 J. Hao, X. Li, S. Zhang, F. Yang, X. Zeng, S. Zhang, G. Bo, C. Wang and Z. Guo, *Adv. Funct. Mater.*, 2020, **30**, 2001263.
23 L. Ma, S. Chen, N. Li, Z. Liu, Z. Tang, J. A. Zapien, S. Chen, J. Fan and C. Zhi, *Adv. Mater.*, 2020, **32**, 1908121.
24 C. Liu, X. Xie, B. Lu, J. Zhou and S. Liang, *ACS Energy Lett.*, 2021, **6**, 1015–1033.
25 F. Yang, J. A. Yuwono, J. Hao, J. Long, L. Yuan, Y. Wang, S. Liu, Y. Fan, S. Zhao and K. Davey, *Adv. Mater.*, 2022, **34**, 2206754.
26 N. Zhang, F. Cheng, Y. Liu, Q. Zhao, K. Lei, C. Chen, X. Liu and J. Chen, *J. Am. Chem. Soc.*, 2016, **138**, 12894–12901.
27 F. Wang, O. Borodin, T. Gao, X. Fan, W. Sun, F. Han, A. Faraone, J. A. Dura, K. Xu and C. Wang, *Nat. Mater.*, 2018, **17**, 543–549.
28 L. Yuan, J. Hao, C.-C. Kao, C. Wu, H.-K. Liu, S.-X. Dou and S.-Z. Qiao, *Energy Environ. Sci.*, 2021, **14**, 5669–5689.
29 O. Borodin, J. Self, K. A. Persson, C. Wang and K. Xu, *Joule*, 2020, **4**, 69–100.
30 X. Li, Z. Chen, P. Ruan, X. Hu, B. Lu, X. Yuan, S. Tian and J. Zhou, *Nanoscale*, 2024, **16**, 2923–2930.
31 X. Xie, J. Li, Z. Xing, B. Lu, S. Liang and J. Zhou, *Natl. Sci.*, 2023, **10**, nwac281.
32 X. Shi, J. Xie, J. Wang, S. Xie, Z. Yang and X. Lu, *Nat. Commun.*, 2024, **15**, 302.
33 L. Cao, D. Li, E. Hu, J. Xu, T. Deng, L. Ma, Y. Wang, X.-Q. Yang and C. Wang, *J. Am. Chem. Soc.*, 2020, **142**, 21404–21409.
34 R. Qin, Y. Wang, M. Zhang, Y. Wang, S. Ding, A. Song, H. Yi, L. Yang, Y. Song and Y. Cui, *Nano Energy*, 2021, **80**, 105478.
35 S. Liu, J. Mao, W. K. Pang, J. Vongsvivut, X. Zeng, L. Thomsen, Y. Wang, J. Liu, D. Li and Z. Guo, *Adv. Funct. Mater.*, 2021, **31**, 2104281.
36 J. Hao, J. Long, B. Li, X. Li, S. Zhang, F. Yang, X. Zeng, Z. Yang, W. K. Pang and Z. Guo, *Adv. Funct. Mater.*, 2019, **29**, 1903605.
37 K. Lu, C. Chen, Y. Wu, C. Liu, J. Song, H. Jing, P. Zhao, B. Liu, M. Xia and Q. Hao, *Chem. Eng. J.*, 2023, **457**, 141287.
38 S. Chen, Q. Nian, L. Zheng, B.-Q. Xiong, Z. Wang, Y. Shen and X. Ren, *J. Mater. Chem. A*, 2021, **9**, 22347–22352.
39 Y. Ma, Q. Zhang, L. Liu, Y. Li, H. Li, Z. Yan and J. Chen, *Natl. Sci.*, 2022, **9**, nwac051.
40 D. Wang, Q. Li, Y. Zhao, H. Hong, H. Li, Z. Huang, G. Liang, Q. Yang and C. Zhi, *Adv. Energy Mater.*, 2022, **12**, 2102707.
41 X. S. Lin, Z. R. Wang, L. H. Ge, J. W. Xu, W. Q. Ma, M. M. Ren, W. L. Liu, J. S. Yao and C. B. Zhang, *Chemelectrochem*, 2022, **9**, e202101724.
42 Y. Lv, Y. Xiao, L. Ma, C. Zhi and S. Chen, *Adv. Mater.*, 2022, **34**, 2106409.
43 Y. Wu, Z. Zhu, D. Shen, L. Chen, T. Song, T. Kang, Z. Tong, Y. Tang, H. Wang and C. S. Lee, *Energy Storage Mater.*, 2022, **45**, 1084–1091.
44 Y. Yang, C. Huang, H. Li, Z. Teng, H. Zhang, X. Wei, H. Zhang, L. Wu, C. Zhang and W. Chen, *J. Mater. Chem. C*, 2023, **11**, 9559.
45 W. Kao-ian, M. T. Nguyen, T. Yonezawa, R. Pornprasertsuk, J. Qin, S. Siwamogsatham and S. Kheawhom, *Mater. Today Energy*, 2021, **21**, 100738.
46 Y. Geng, L. Pan, Z. Peng, Z. Sun, H. Lin, C. Mao, L. Wang, L. Dai, H. Liu and K. Pan, *Energy Storage Mater.*, 2022, **51**, 733–755.
47 J. Li, Z. Liu, S. Han, P. Zhou, B. Lu, J. Zhou, Z. Zeng, Z. Chen and J. Zhou, *Nano-Micro Lett.*, 2023, **15**, 237.
48 T. Lu and Q. Chen, *J. Comput. Chem.*, 2022, **43**, 539–555.
49 N. Chang, T. Li, R. Li, S. Wang, Y. Yin, H. Zhang and X. Li, *Energy Environ. Sci.*, 2020, **13**, 3527–3535.
50 Y. Dong, L. Miao, G. Ma, S. Di, Y. Wang, L. Wang, J. Xu and N. Zhang, *Chem. Sci.*, 2021, **12**, 5843–5852.
51 J.-B. Brubach, A. Mermet, A. Filabozzi, A. Gerschel, D. Lairez, M. Krafft and P. Roy, *J. Phys. Chem. B*, 2001, **105**, 430–435.
52 H. Du, R. Zhao, Y. Yang, Z. Liu, L. Qie and Y. Huang, *Angew. Chem.*, 2022, **134**, e202114789.
53 Y. Zhu, J. Hao, Y. Huang and Y. Jiao, *Small Struct.*, 2023, **4**, 2200270.
54 Q. Sun, *Vib. Spectrosc.*, 2009, **51**, 213–217.
55 C. Li, Z. Sun, T. Yang, L. Yu, N. Wei, Z. Tian, J. Cai, J. Lv, Y. Shao and M. H. Rümmeli, *Adv. Mater.*, 2020, **32**, 2003425.
56 D. Mackinnon, J. Brannen and P. Fenn, *J. Appl. Electrochem.*, 1987, **17**, 1129–1143.
57 B. Tripathy, S. Das, G. Hefter and P. Singh, *J. Appl. Electrochem.*, 1997, **27**, 673–678.
58 Q. Zhang and Y. Hua, *J. Appl. Electrochem.*, 2009, **39**, 261–267.
59 D. Mackinnon, R. Morrison, J. Mouland and P. Warren, *J. Appl. Electrochem.*, 1990, **20**, 728–736.
60 A. Pei, G. Zheng, F. Shi, Y. Li and Y. Cui, *Nano Lett.*, 2017, **17**, 1132–1139.
61 M. Frish, G. Trucks, H. Schlegel, G. Scuseria, M. Robb, J. Cheeseman, G. Scalmani, V. Barone, B. Mennucci and G. Paterson, *Gaussian09*, Gaussian, Inc., Wallingford CT, 2009, vol. 121, pp. 150–166.
62 M. P. Andersson and P. Uvdal, *J. Phys. Chem. A*, 2005, **109**, 2937–2941.
63 T. Lu and F. Chen, *J. Comput. Chem.*, 2012, **33**, 580–592.

64 W. Humphrey, A. Dalke and K. Schulten, *J. Mol. Graph. Model.*, 1996, **14**, 33–38.
65 T. Williams, C. Kelley, C. Bersch, H.-B. Bröker, J. Campbell, R. Cunningham, D. Denholm, G. Elber, R. Fearick and C. Grammes, *An Interactive Plotting Program*, 2017, vol. 2, p. 1, available online: **http://www.gnuplot.info/docs_5**.
66 S. Simon, M. Duran and J. Dannenberg, *J. Chem. Phys.*, 1996, **105**, 11024–11031.
67 J. C. Phillips, R. Braun, W. Wang, J. Gumbart, E. Tajkhorshid, E. Villa, C. Chipot, R. D. Skeel, L. Kale and K. Schulten, *J. Comput. Chem.*, 2005, **26**, 1781–1802.
68 J. Huang and A. D. MacKerell Jr, *J. Comput. Chem.*, 2013, **34**, 2135–2145.
69 P. Mark and L. Nilsson, *J. Phys. Chem. A*, 2001, **105**, 9954–9960.
70 S. E. Feller, Y. Zhang, R. W. Pastor and B. R. Brooks, *J. Chem. Phys.*, 1995, **103**, 4613–4621.
71 S. Nosé, *Mol. Phys.*, 1984, **52**, 255–268.
72 T. D. Kühne, M. Iannuzzi, M. Del Ben, V. V. Rybkin, P. Seewald, F. Stein, T. Laino, R. Z. Khaliullin, O. Schütt and F. Schiffmann, *J. Chem. Phys.*, 2020, **152**, 194103.
73 J. VandeVondele, M. Krack, F. Mohamed, M. Parrinello, T. Chassaing and J. Hutter, *Comput. Phys. Commun.*, 2005, **167**, 103–128.
74 J. P. Perdew, K. Burke and M. Ernzerhof, *Phys. Rev. Lett.*, 1996, **77**, 3865.
75 M. A. Marques, M. J. Oliveira and T. Burnus, *Comput. Phys. Commun.*, 2012, **183**, 2272–2281.
76 J. VandeVondele and J. Hutter, *J. Chem. Phys.*, 2007, **127**, 114105.
77 S. Goedecker, M. Teter and J. Hutter, *Phys. Rev. B: Condens. Matter Mater. Phys.*, 1996, **54**, 1703.
78 R. Jonchiere, A. P. Seitsonen, G. Ferlat, A. M. Saitta and R. Vuilleumier, *J. Chem. Phys.*, 2011, **135**, 154503.
79 S. Grimme, J. Antony, S. Ehrlich and H. Krieg, *J. Chem. Phys.*, 2010, **132**, 154104.